Numerical Investigation of a Solar Sunrise Transient Temperature Model for Latent Heat Thermal Energy Storage System#

Raymond O. Ikeleji[1*], Tunde Bello-Ochende[1]

[1]Department of Mechanical Engineering, University of Cape Town, Private Bag X3, Rondebosch, 7701, South Africa

(*Corresponding Author: iklray001@myuct.ac.za)

ABSTRACT

This study investigates numerically the sunrise and sunset transient temperature model that is developed for modeling sunlight's temperature in designing latent heat thermal energy storage system (LHTESS), to close carbon cycles. It was used as a model for the three-dimensional conjugate phase change material (PCM) melting procedure in the thermal storage of a 500K-rated concentrated solar power (CSP) plant using computational fluid dynamics (CFD) code. Air is the heat transfer fluid (HTF). Two transient solar temperature models and an isothermal model were studied and compared. The reduction in the expected storage time and increased energy storage greatly improved the system's efficiency. The numerical model results were substantiated by experimental evidence from the open literature.

Keywords: CSP, CFD, PCM, LHTESS, Heat transfer, Sunrise and Sunset temperature model.

NOMENCLATURE

Abbreviations	
TES	Thermal energy storage
CSP	Concentrated solar power
CFD	Computational fluid dynamics
Symbols	
h	hour
m	minutes
ρ	Density kg/m^3
λ	Liquid fraction
L	Latent heat kJ/kg
T_m	Melting temperature ^0C
A_{mush}	Mushy zone constant
μ	Dynamic viscosity $kg/m\,s$
C_p	Specific heat capacity $J/kg\,K$

1. INTRODUCTION

A mitigation technique has been the TES in PCMs due to the low density and transitory characteristics of the sun in (CSP) plants [1]. The energy which is released on demand or during off-peaks is constrained by the poor thermal conductivities of PCMs which vary from 0.2 W/m K and 0.7 W/m K and cause very slow energy storage over a prolonged length of time while charging [2]. This thermal system's effectiveness is consequently constrained by this. The utilization of metal inserts with high thermal conductivity, heat pipes (HPs), nanofluids, encapsulation, and fins were some of the suggested existing enhancement techniques as remedies [3–5]. The need for optimal performance of the energy bank has been a central heat transfer issue that is still being researched. Some of the heat transfer enhancement approaches have been documented in the literature.

PCM-filled metal foam configuration has found very useful applications as an enhancer. Atal et al [3] evaluated the impact of 95% and 77% aluminium metal foam porosities on the thermal efficiency of an LHTESS using numerical and experimental approaches. The thermal system was examined in five different configurations. The foam with reduced porosity (higher metal content) improved the charge and discharge cycles more, because of its better thermal conductivity. A computer model for PCM incorporated into metal foam was created by Liu et-al [4] and used to examine PCM transition in a shell-and-tube LHTESS. The authors reported more than seven times improvement in heat transfer. Furthermore, the charge and discharge time was reduced when 5% copper nanoparticles were added to metal foam with various nanoparticle concentrations and porosities in a triple-tube LHTESS [5]. The study demonstrated metal foam's benefit as an additive rather than nanoparticles.

Heat pipes and fins are regarded to be one of the most effective enhancers. Sharifi et-al [6] numerically modeled

the melting of a PCM in a vertical cylinder and heat pipes and reported that HPs function better from an isothermal surface, making them the preferable choice for enhancing heat transfer in LHTESS. The authors created a model that predicts an increase in charging caused by the use of the HPs and orientations. Nithyandam and Pitchumani [7] carried out a comprehensive computational evaluation of an LHTESS with embedded HPs in three dimensions. The authors discovered that HPs were quite effective during the charge and discharge procedures. To investigate heat transmission in an LHTESS for electricity generation, Shabgard [8] created a thermal network model to quantify the enhancement brought on by including HPs during PCM charge and discharge processes.

Reference [9–11] is recommended for further studies on heat pipes and [12] extensively reviewed heat transfer enhancement methods for LHTES in solar heating systems. Reference [13–17] exhaustively studied and reported the importance of fins as an effective heat transfer enhancer in TES systems.

For the encapsulation approach, Mallya and Haussener [18] quantitatively studied encapsulated PCM with constant temperature walls in both vertical and horizontal orientations, charge and discharge processes, and heat transfer media. Their findings quantified the impact of HPs on the boundary conditions, thermophysical characteristics, geometrical parameters, and natural convection in spherically encapsulated PCMs. Amin et-al [19] proved through experimentation and numerical analysis the validity of establishing an empirical relationship for the heat transfer in PCM contained in spherical encapsulations as an enhancement.

In this study, the sunrise transient temperature model that we developed is applied to model the temperature of the sun in a cylinder and heat pipe CSP thermal storage device. This is aimed at the assessment of the model to determine its efficacy as a heat transfer enhancer for designing high-temperature LHTES systems.

Moreso, to contribute to the existing PCM poor thermal conductivity enhancement techniques. This technology will also contribute to mitigating the transitory characteristics of renewable solar energy resources to close carbon cycles. The heat transfer medium is air. The projected outcome profiles of two transient temperature models and a steady or isothermal model were examined.

2. THE GEOMETRICAL AND COMPUTATIONAL MODEL

The modified three-dimensional model described by [3] was engaged in the study. The cylinder diameter is 0.0508m and the length is 0.3048m. The heat pipe diameter is 5×10^{-3}m and 0.762m long. To develop a uniform inlet flow and avoid backflow pressure, the HP is kept longer at both the inlet and outlet. The heat pipe is made of aluminium and the cylinder is a plexiglass. Table 1 lists the material characteristics. Fig. 1 depicts the computational domain and structured grids. 11000 elements were used to represent the solution field from the grid refinement studies. The cylinder is filled with 0.4186kg of Paraffin wax with the HP embedded while solar-heated air HTF flows through at 0.5 m/s.
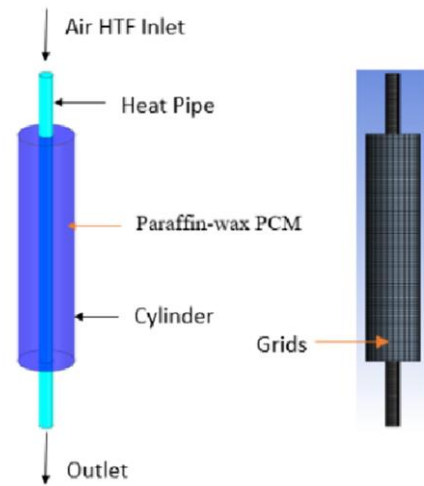

Fig. 1 Computational Domain and Grids

Table 1 Thermophysical properties of materials[3,20,21].

Property	Paraffin Wax		Air	Aluminium	Plexiglass
	Liquid	Solid	(HTF)	(heat pipe)	(shell)
$\rho \ [kg/m^3]$	730	790	-	2719	1180
$C_p \ [J/kg \, K]$	2510		1006.43	871	1470
$k \ [W/mK]$	0.25		0.0242	202.4	0.19
$\mu \ [kg/m \, s]$	1.52915×10^3		1.7894×10^{-5}	-	-
$\beta \ [K^{-1}]$	3.357×10^3		-	-	-
$L \ [KJ/kg]$	117		-	-	-
$T_m \ [^\circ C]$	50	60	-	-	-

3. NUMERICAL MODEL

The enthalpy–porosity technique and the finite volume method as described by [22,23] were used in the CFD simulation which was performed using the commercial fluid dynamics program ANSYS [21].

The Navier-stokes equations were solved by using fluent melting and solidification model to simulate conjugate fluid flow and phase change heat transfer processes. For pressure–velocity coupling, Semi-Implicit Pressure-Linked Equations (SIMPLE) algorithm was employed. The convective terms in the momentum and energy equations were transiently discretized using a second-order upwind differencing approach. For pressure interpolation at the cell faces, the PRESTO scheme was utilized. To achieve steady convergence, momentum, pressure, and liquid fraction were each under-relaxed with 0.5, 0.3, and 0.9 factors. For the continuity, momentum, and energy equations, the residual value was set to 10^{12}.

The time step was set to 0.1s and a liquid fraction of 1 was achieved within 400,000 to 500,000 iterations for the models in 25 hours of high-performance computations for each simulation run. The number of iterations at each time step was set to 1. Several simulations with both grid refinement and parametric studies were done and analysed to ensure that the melting process is completed within the stipulated time. To simulate natural convection, we set the gravity vector in the y-direction to -9.8 m/s^2. The heat pipe was modeled as a solid metal conductor [24].

3.1 Assumptions
The PCM is isotropic and homogeneous while the fluid flow is unsteady, laminar, and three-dimensional. and. PCM volume expansion is neglected during melting. The phase change process is non-linear and time-dependent with coupled fluid flow with heat transfer.
The CSP collector is 500K-rated [25]

3.2 Preliminary boundary conditions

The PCM is characterized as a fluid zone. The system was initially at a temperature of 298.15K in a solid state. Constant thermophysical material properties are assumed for the PCM. The liquid PCM motion is laminar, unsteady, and incompressible. Both heat pipe and cylinder walls are thin, thermally stratified, stationary, no-slip, and adiabatic. A Conjugate interface exists between the HTF, HP, and PCM.

3.3 Governing equations

The three-dimensional conservation of mass, momentum, and energy equations for fluid flow and heat transfer in terms of sensible enthalpy is below.

3.3.1 Continuity equation

The conservation of mass or energy is defined by.

$$\frac{\partial(\rho u)}{\partial t} + \frac{\partial(\rho u v)}{\partial y} + \frac{\partial(\rho u w)}{\partial y} = 0 \qquad (1)$$

3.3.2 Energy equation

$$H = h + \Delta H \qquad (2)$$

$$h = h_{ref} + \int_{T_{ref}}^{T} c_p \partial T \qquad (3)$$

h_{ref} is the reference enthalpy, T_{ref} is the reference temperature, and c_p is the specific heat at constant pressure.
The liquid fraction λ is defined by.

$$\lambda = \begin{cases} 0 & T < T_{Solidus} \\ \dfrac{T - T_{Solidus}}{T_{Liquidus} - T_{Solidus}} & T_{Solidus} \leq T \leq T_{Liquidus} \\ 1 & T > T_{Liquidus} \end{cases} \qquad (4)$$

And the latent heat content L is defined in terms of the material latent heat L by.

$$\Delta H = \lambda L \qquad (5)$$

The latent heat content can vary between 0 and 1 for solid and liquid respectively.

3.3.3 Energy equation

$$\frac{\partial(\rho H)}{\partial t} + \frac{\partial(\rho u H)}{\partial x} + \frac{\partial(\rho v H)}{\partial y} + \frac{\partial(\rho w H)}{\partial z} =$$

$$-\frac{\partial}{\partial x}\left(k\frac{\partial T}{\partial x}\right) + \frac{\partial}{\partial y}\left(k\frac{\partial T}{\partial y}\right) + \frac{\partial}{\partial z}\left(k\frac{\partial T}{\partial z}\right) + S_e \quad (6)$$

H, ρ, k and t are the PCM enthalpy, density, and thermal conductivity, while S_e is energy equation volumetric latent heat source term defined by [26].

$$s_e = \frac{\partial \Delta H}{\partial t} \qquad (7)$$

3.3.4 Momentum equations

x-momentum

$$\frac{\partial(\rho u)}{\partial t}+\frac{\partial(\rho uu)}{\partial x}+\frac{\partial(\rho uv)}{\partial y}+\frac{\partial(\rho uw)}{\partial z}=$$

$$-\frac{\partial P}{\partial x}+\frac{\partial}{\partial x}\left(\mu\frac{\partial u}{\partial x}\right)+\frac{\partial}{\partial y}\left(\mu\frac{\partial u}{\partial y}\right)+\frac{\partial}{\partial z}\left(\mu\frac{\partial u}{\partial z}\right)+S_x \quad (8)$$

where ρ is the PCM density; μ is the PCM viscosity; u v and w are PCM superficial velocities in x, y and z directions respectively.

y-momentum

$$\frac{\partial(\rho v)}{\partial t}+\frac{\partial(\rho uv)}{\partial x}+\frac{\partial(\rho vv)}{\partial y}+\frac{\partial(\rho vw)}{\partial z}=$$

$$-\frac{\partial P}{\partial y}+\frac{\partial}{\partial x}\left(\mu\frac{\partial v}{\partial x}\right)+\frac{\partial}{\partial y}\left(\mu\frac{\partial v}{\partial y}\right)+\frac{\partial}{\partial z}\left(\mu\frac{\partial v}{\partial z}\right)+S_y \quad (9)$$

z-momentum

$$\frac{\partial(\rho w)}{\partial t}+\frac{\partial(\rho uw)}{\partial x}+\frac{\partial(\rho vw)}{\partial y}+\frac{\partial(\rho ww)}{\partial z}=$$

$$-\frac{\partial P}{\partial w}+\frac{\partial}{\partial x}\left(\mu\frac{\partial w}{\partial x}\right)+\frac{\partial}{\partial y}\left(\mu\frac{\partial w}{\partial y}\right)+\frac{\partial}{\partial w}\left(\mu\frac{\partial w}{\partial z}\right)+S_w+S_b \quad (10)$$

The momentum sinks; $S_x=-A_{mush}(\lambda)u$, $S_y=-A_{mush}(\lambda)v$ and $S_z=-A_{mush}(\lambda)w$ due to the reduced porosity in the mushy zone mimics the Carman-Kozeny equation derived from Darcy law for fluid flow in porous media defined by.

$$S_x=1-\frac{(1-\lambda)^2}{\lambda^3+\varepsilon}A_{mush}$$

$$S_y=1-\frac{(1-\lambda)^2}{\lambda^3+\varepsilon}A_{mush} \quad (11)$$

$$S_z=1-\frac{(1-\lambda)^2}{\lambda^3+\varepsilon}A_{mush}$$

A_{mush} , λ and ε are mushy zone constant, liquid volume fraction, and Carman-Kozeny equation constant which is a small number (ε = 0.001) that prevents division by zero in the denominator). $A_{mush}(\lambda)$ is the ''porosity function'' defined by[27]. $A_{mush}=10^5$ [21] was used in this design. With the Boussinesq model, natural convection in the melt is modeled. Except for the body force term, the momentum equation is modeled under the assumption that fluid density is constant. This is defined by the buoyancy source term below.

$$S_b=\rho g\beta(T-T_m) \quad (12)$$

g , β , T_m and T are the PCM viscosity, volumetric expansion coefficient, reference density, melting temperature, and transient solar temperature respectively.

4. VALIDATION OF NUMERICAL MODEL RESULTS

The experimental work from [3] was employed to verify the results of the numerical model and the predictions agreed well. The comparison of the simulation result for the PCM right-mid-temperature distribution is depicted in Fig. 2. Using the equation from [28], the behaviour of the liquid fraction evolution during charge and discharge cycles is accurately predicted to be within 0.04%.
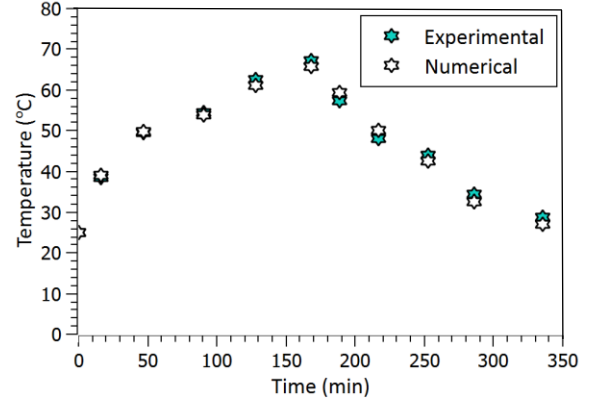

Fig. 2 Numerical model validation.

5. RESULTS AND DISCUSSIONS
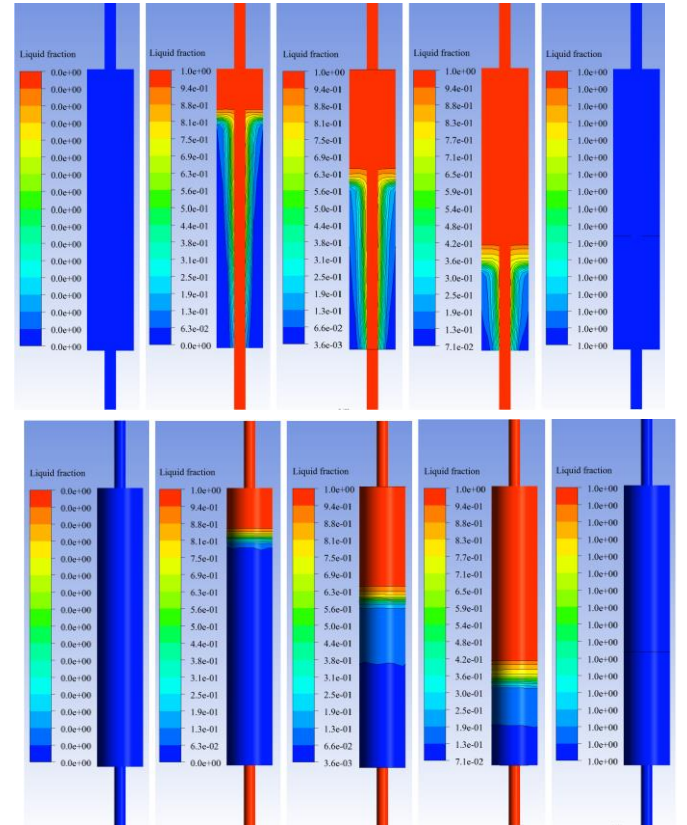
5.1 Contours

Fig. 3 Model-2 Liquid fraction contour

The predicted liquid fraction evolution for Model-2 indicating liquid, mushy, and solid regions is reported in Fig. 3 in two and three dimensions. From left to right show the melt fraction at 0.25, 0.5, 0.75, and 1 at 3h 12m, 3h 48m, 4h 33m, and 6h 30m respectively. Natural convection expedites the melting process as seen from the short time interval between 0.25 and 0.5 melt stage. Conduction heat transfer dominated the process afterward and account for a slow melting process.

5.2 Solar temperature source models
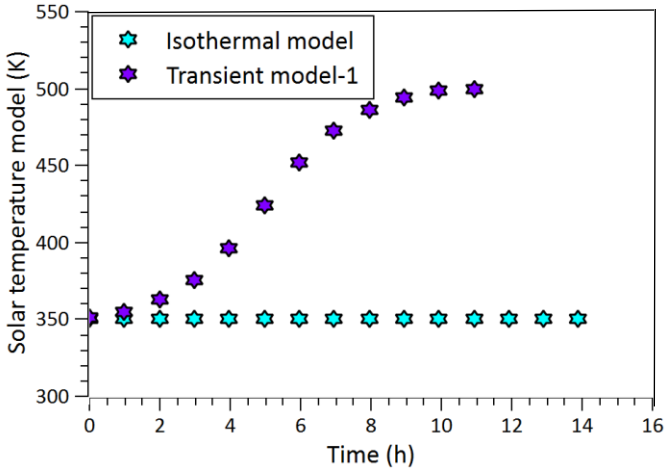
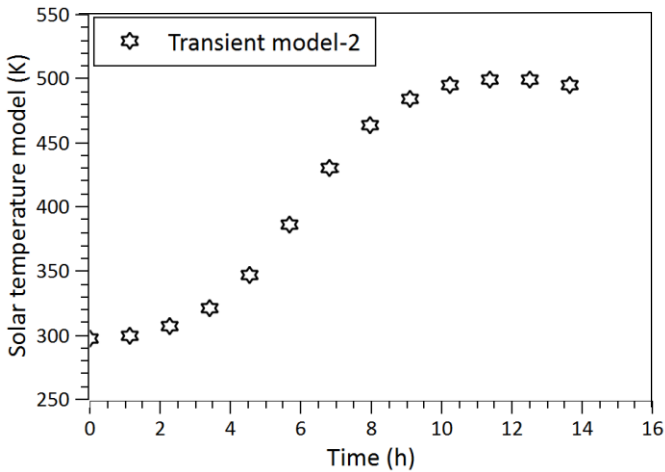Fig. 4a Solar transient model-1 and isothermal model

Fig. 4b Solar transient Model-2

The profiles for the three solar temperature source models are shown in Fig. 4a and Fig. 4b. They consist of two transient solar temperature models referred to as Model-1 and Model-2, and a steady or isothermal solar temperature model. Transient model-1 is compared with the steady model, with both models having the same inlet temperature of 350K as shown in the profiles of Fig. 4a. This temperature is selected based on the maximum safe and stable solver allowable HTF inlet temperature for this configuration. While the model-1 temperature rises simultaneously with solar sunrise temperature to 500 K solar collector temperature rating, the steady temperature model remains constant at 350K during the simulation. This temperature is above the PCM initial temperature of 298K respectively.

Transient model-2 in Fig. 4b has an ambient inlet HTF temperature of 298K that corresponds to the PCM solidus temperature. As the sun's intensity increases, the temperature rises in tandem with the 500k solar collector rating and transfers heat to melt the PCM. The inlet temperature is the basic distinction between both model-1 and model-2.
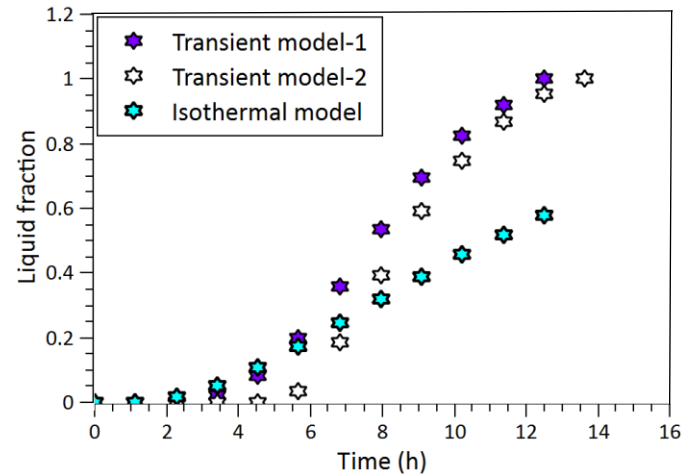
5.3 The Liquid fraction

Fig. 5 Liquid fractions

The transient variation of the PCM liquid fraction for transient model-1, model-2, and the isothermal model is in Fig. 5. Model-1 require an average of 11h 55m to completely melt with a liquid volume fraction of 1, while the isothermal model, the liquid volume fraction is 0.55 at the same time, with 45.5% difference. This is a significant improvement with the predicted transient model-1. With transient model-2, the liquid volume fraction is 0.91 at the same time and melts completely with a liquid volume fraction of 1, in 13h 38m. Liquid fraction for the steady model at the end of the simulation run is 0.64 in 13h 53m. This demonstrates the superiority of the proposed transient models and the efficacy and applicability of the transient source model in LHTESS design.

The energy curve in Fig. 6 illustrates the profiles for the amount of stored solar energy for the models with time. For model-1 the maximum stored energy is 0.402MW when the liquid fraction is 1 in 11h 55m. This is 71.5% more when compared with the 0.1623MW in 13h 53m for the isothermal model. Comparatively, the amount of solar

energy stored with model-2 is superior, at 0.413 MW in 13h 38m. This further suggests heat transfer enhancement with the predicted transient model.
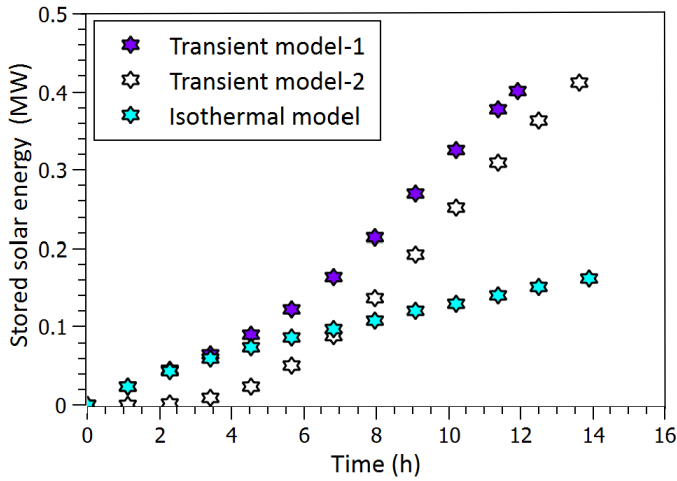
5.4 Stored solar energy and temperature
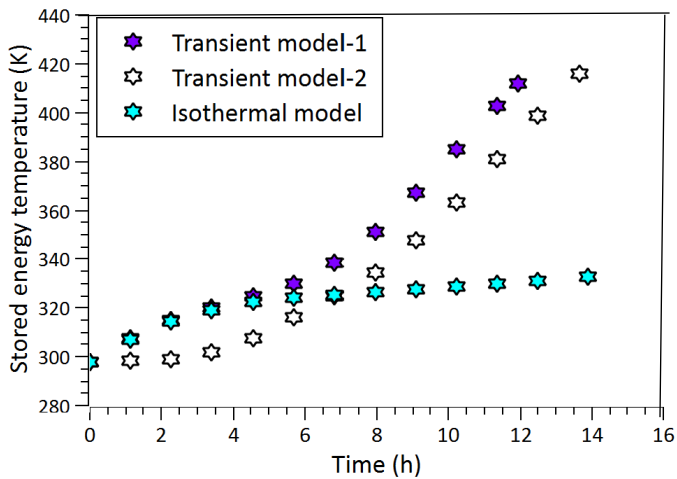

Fig. 6 Energy curve

Fig. 7 Stored solar energy temperature

The corresponding temperatures for the Paraffin-wax PCM for model-1, isothermal, and model-2 are 388.9434K, 332.7549K, and 435.7802K respectively. The temperature profiles are illustrated in Fig. 7.

6. CONCLUSION

The predicted sunrise transient temperature model expedites the charging process and was more effective. It could be considered a promising technique when combined with other enhancers in the design of more efficient high-temperature thermal storage for industrial and domestic applications such as electricity generation, heating and cooking within eight hours [29] of solar insolation.

CRediT authorship contribution statement
Raymond O. Ikeleji: Conception, Methodology, Data Analysis, Validation. Original draft, Review, and Editing of writing.

Tunde Bello-Ochende: Software, Methodology, Review and Supervision

Declaration of competing interest
The authors affirm that they have no known financial conflicts of interest or close personal ties that might have seemed to affect the work disclosed in this article and submission for publication.

Data availability
The investigation detailed in the article does not involve any external data.

REFERENCE

[1] Tian Y, Zhao CY. A review of solar collectors and thermal energy storage in solar thermal applications. Applied Energy 2013; 104:538–53.

[2] Sharifi N, Faghri A, Bergman TL, Andraka CE. Simulation of heat pipe-assisted latent heat thermal energy storage with simultaneous charging and discharging. International Journal of Heat and Mass Transfer 2015; 80:170–9.

[3] Atal A, Wang Y, Harsha M, Sengupta S. Effect of porosity of conducting matrix on a phase change energy storage device. International Journal of Heat and Mass Transfer 2016; 93:9–16.

[4] Liu Z, Yao Y, Wu H. Numerical modeling for solid-liquid phase change phenomena in porous media: Shell-and-tube type latent heat thermal energy storage. Applied Energy 2013; 112:1222–32.

[5] Li Z, Shahsavar A, Al-Rashed AAAA, Talebizadehsardari P. Effect of porous medium and nanoparticles presence in a counter-current triple-tube composite porous/nano-PCM system. Applied Thermal Engineering 2020;167.

[6] Sharifi N, Wang S, Bergman TL, Faghri A. Heat pipe-assisted melting of a phase change material. International Journal of Heat and Mass Transfer 2012; 55:3458–69.

[7] Nithyanandam K, Pitchumani R. Computational studies on a latent thermal energy storage system with integral heat pipes for concentrating solar power. Applied Energy 2013; 103:400–15.

[8] Shabgard H, Bergman TL, Sharifi N, Faghri A. High temperature latent heat thermal energy storage using heat pipes. International Journal of Heat and Mass Transfer 2010; 53:2979–88.

[9] Nithyanandam K, Pitchumani R. Thermal energy storage with heat transfer augmentation using thermosyphons. International Journal of Heat and Mass Transfer 2013; 67:281–94.

[10] Nithyanandam K, Pitchumani R. Design of a latent thermal energy storage system with embedded heat pipes. Applied Energy 2014; 126:266–80.

[11] Nithyanandam K, Pitchumani R. Analysis and optimization of a latent thermal energy storage system with embedded heat pipes. International Journal of Heat and Mass Transfer 2011; 54:4596–610.

[12] Liu W, Bie Y, Xu T, Cichon A, Królczyk G, Li Z. Heat transfer enhancement of latent heat thermal energy storage in the solar heating system: A state-of-the-art review. Journal of Energy Storage 2022;46.

[13] Mehta DS, Vaghela B, Rathod MK, Banerjee J. Heat transfer enhancement using spiral fins in different orientations of Latent Heat Storage Unit. International Journal of Thermal Sciences 2021;169.

[14] Mahdi JM, Nsofor EC. Melting enhancement in triplex-tube latent thermal energy storage system using nanoparticles-fins combination. International Journal of Heat and Mass Transfer 2017; 109:417–27.

[15] Yang X, Lu Z, Bai Q, Zhang Q, Jin L, Yan J. Thermal performance of a shell-and-tube latent heat thermal energy storage unit: Role of annular fins. Applied Energy 2017;202:558–70.

[16] Zonouzi SA, Dadvar A. Numerical investigation of using helical fins for the enhancement of the charging process of a latent heat thermal energy storage system. Journal of Energy Storage 2022;49.

[17] Huang Y, Cao D, Sun D, Liu X. Experimental and numerical studies on the heat transfer improvement of a latent heat storage unit using gradient tree-shaped fins. International Journal of Heat and Mass Transfer 2022;182.

[18] Mallya N, Haussener S. Buoyancy-driven melting and solidification heat transfer analysis in encapsulated phase change materials. International Journal of Heat and Mass Transfer 2021; 164:120525.

[19] Amin NAM, Bruno F, Belusko M. Effective thermal conductivity for melting in PCM encapsulated in a sphere. Applied Energy 2014; 122:280–7.

[20] Fadl M, Eames PC. Numerical investigation of the influence of mushy zone parameter A_{mush} on heat transfer characteristics in vertically and horizontally oriented thermal energy storage systems. Applied Thermal Engineering 2019;151:90–9.

[21] ANSYS Fluent Theory Guide. 2017.

[22] Patankar Sulhas V. Numerical Heat Transfer and Fluid Flow. New York: McGraw-Hill; 1980.

[23] Voller VR, Swaminathan CR. General source-based method for solidification phase change. Numerical Heat Transfer, Part B: Fundamentals 1991;19:175–89.

[24] Tiari S, Qiu S, Mahdavi M. Numerical study of finned heat pipe-assisted thermal energy storage system with high-temperature phase change material. Energy Conversion and Management 2015; 89:833–42.

[25] Ebadi S, Tasnim SH, Aliabadi AA, Mahmud S. Melting of nano-PCM inside a cylindrical thermal energy storage system: Numerical study with experimental verification. Energy Conversion and Management 2018; 166:241–59.

[26] Voller VR, Prakash C. A fixed grid numerical modeling methodology for convection-diffusion mushy region phase-change problems. vol. 30. 1987.

[27] Brent AD, Voller VR, Reid KJ. Enthalpy-porosity technique for modeling convection-diffusion phase change: Application to the melting of a pure metal. Numerical Heat Transfer 1988; 13:297–318.

[28] Guang W, Baraldo M, Furlanut M. Calculating percentage prediction error: A user's note. Pharmacological Research 1995; 32:241–8.

[29] Cárdenas B, León N, Pye J, García HD. Design and modeling of a high temperature solar thermal energy storage unit based on molten soda lime silica glass. Solar Energy 2016; 126:32–43.